


# Selective energy filtering in a multiple-quantum-well nanodevice: The quantum cascade cooler

Guéric Etesse<sup>1,\*</sup>, Chloé Salhani,<sup>2,3</sup> Xiangyu Zhu,<sup>2</sup> Nicolas Cavassilas,<sup>1</sup> Kazuhiko Hirakawa,<sup>2,3</sup> and Marc Bescond<sup>1,2,†</sup>

<sup>1</sup>*IM2NP, UMR CNRS 7334, Aix-Marseille Université, Technopôle de Château-Gombert, Bâtiment Néel, 60 Rue Frédéric Joliot Curie, Marseille 13453, France*

<sup>2</sup>*Institute of Industrial Science, University of Tokyo, 4-6-1 Komaba, Meguro-ku, Tokyo 153-8505, Japan*

<sup>3</sup>*LIMMS-CNRS, IRL 2820, 4-6-1 Komaba, Meguro-ku, Tokyo 153-8505, Japan*

 (Received 29 August 2023; revised 8 March 2024; accepted 9 April 2024; published 6 May 2024)

Using quantum transport simulations, we study the operating principle of a proposed quantum cascade cooler, a multiple-quantum-well structure whose cooling capabilities rely on combined resonant tunneling and thermionic-emission filtering. We couple charge and heat transport by self-consistently solving nonequilibrium Green's functions and the heat equation, and we subsequently calculate the thermodynamic properties of the electrons using noninvasive virtual probes. We show that this device exhibits bias-dependent electron-temperature oscillations emerging from electron-phonon interactions and inter-subband transitions. Finally, we show the advantages of a multiple-quantum-well structure over a single quantum well and discuss the actual potential for such a structure to effectively cool down the crystal lattice upon optimization.

DOI: [10.1103/PhysRevApplied.21.054010](https://doi.org/10.1103/PhysRevApplied.21.054010)

## I. INTRODUCTION

In the last few decades, the need for improved heat-management devices and systems has become a major challenge for both energetic and environmental reasons, as well as to avoid technical limitations on state-of-the-art electronic devices. For instance, in the information and communications technology (ICT) sector, the increasing demand for data centers has resulted in their energy consumption reaching an estimated 1.4% of total worldwide energy consumption, of which almost half is used solely for cooling purposes [1,2]. The carbon footprint of such facilities is estimated to be experiencing the highest growth rate across the whole ICT sector [3], being responsible for 2% of CO<sub>2</sub> emissions, a proportion comparable to that of the aviation sector [3].

Modern microchips have continued to follow Moore's law, which states that the transistor counts of integrated circuits will double every 2 years [4–6], and we have now attained transistor densities of the order of a billion devices per chip. The associated power densities are, hence, becoming dangerously close to values that are hard to administer without substantial enhancements in cooling processes, leading to the appearance of software limitations on the clock speeds of some recent processors [4,7].

Current active heat-dissipation methods, including faning and liquid cooling, have the advantage of large coefficients of performance [8]. However, they lack the compactness and silence required for portable devices [9]. More importantly, the appearance of hot spots due to the miniaturization of electronic devices down to sizes comparable with the phonon mean free path [10–12] cannot be properly addressed by these types of approach. Indeed, they rely on the extraction of heat diffused to a heat sink and therefore cannot deal with the nonuniformity of temperature emerging from localized hot spots.

Thermoelectric refrigeration systems using the Peltier effect [13] have been investigated as a possible solution to address these hot spots. However, their size, which is of the order of a few hundred micrometers, induces a significant amount of scattering amongst the electrons, which in turn leads to a reduced power factor  $S^2\sigma$ , where  $S$  is the Seebeck coefficient and  $\sigma$  is the electrical conductivity. One potential approach to overcoming these scattering issues is thermionic refrigeration [14]. Within this approach, electrons absorb heat from the cathode [15] and are thermionically transmitted to the anode before scattering processes can take place. It has also been observed that with this mechanism, it is possible for a semiconductor heterostructure at room temperature to directly cool down the electrons before they transfer their energy to the lattice [16].

The asymmetric double-barrier heterostructure originally proposed by Chao *et al.* [17] takes advantage of

\*Corresponding author: [gueric.ettesse@im2np.fr](mailto:gueric.ettesse@im2np.fr)

†Corresponding author: [bescond@iis.u-tokyo.ac.jp](mailto:bescond@iis.u-tokyo.ac.jp)

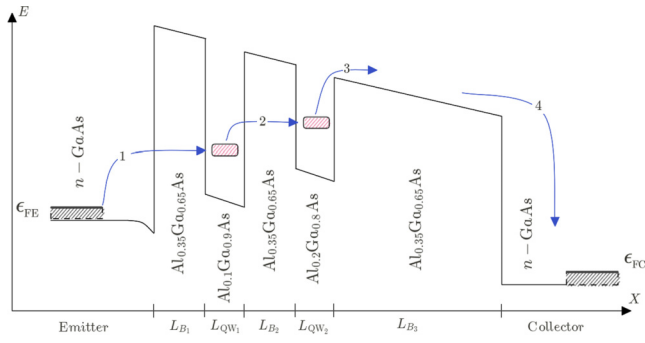


FIG. 1. Considered quantum cascade cooler with  $L_{B_1} = L_{B_2} = 6$  nm,  $L_{QW_1} = L_{QW_2} = 5$  nm, and  $L_{B_3} = 30$  nm. The solid black line corresponds to the edge of the conduction band. Here  $\epsilon_{FE}$  and  $\epsilon_{FC}$  are the Fermi levels of the emitter and collector, respectively. The ground states of the quantum wells are described by the red-hatched rounded rectangles. The intended working principle is represented by the successive blue arrows and is decomposed into four steps. (1) Electrons are injected from the emitter in the first quantum well (QW1) by resonant tunneling. (2) Electrons are injected into the second quantum well (QW2) by phonon-assisted tunneling. (3) Electrons are thermionically extracted from the second quantum well. (4) Electrons are progressively relaxed in the collector through electron-phonon interactions.

resonant tunneling across an initial thin barrier and restricts the injection to cold electrons. It has been shown by Yan-gui *et al.* that the thermionic emission from a quantum well (QW) can lead to substantial evaporative cooling of electrons up to 50 K below room temperature [16]. In the present work, we propose and theoretically investigate an AlGaAs-based heterostructure, as shown in Fig. 1, derived from an asymmetric double barrier and consisting of sequentially stacked QWs. With appropriate band engineering, it is possible to progressively increase the energy levels of successive QW states. In this configuration, an electron absorbing a phonon in the first QW can tunnel into the next QW of the structure, where another phonon can be absorbed. Electrons are finally extracted from the last QW by thermionic emission over a thicker layer, which acts as a thermal wall to prevent heat back-flow. This process is similar to that occurring in a quantum cascade laser [18] between electron and photon emission, which leads us to identify this structure as a “quantum cascade cooler” (QCC). The role of the successive barriers is to filter injected electrons and to concentrate the cooling in the QWs. By doing so, we will be able to precisely refrigerate nanoscale regions and to present a proof of concept to address the hot-spot issue. This type of solution will need to be adapted to the specifics of the device it aims to cool, depending on its materials and the type of circuit conception. The exact general application of these nanocoolers is, however, beyond the scope of the present article.

Using quantum transport code based on the nonequilibrium Green’s functions formalism coupled to the heat

equation, we show that the electron temperature in each QW exhibits anticorrelated oscillations as a function of the applied voltage. Simulations show that these temperature oscillations depend on the energy difference between two consecutive QW states and are directly linked to the polar-optical-phonon energy.

The remainder of this paper is organized as follows. Section II presents the theoretical framework used to compute the electron and heat transport as well as the local thermodynamic properties of the electrons. Section III develops the physical analysis associated with the studied structure. Finally, Sec. IV concludes this work by summarizing the key findings.

## II. THEORETICAL APPROACH

We consider the heterostructure represented in Fig. 1, whose emitter (cathode) and collector (anode) regions are  $n$ -doped GaAs layers with a donor concentration of  $10^{18}$  cm $^{-3}$ . The undoped active region is composed of five layers: we consider two 5-nm-thick QWs composed of Al $_{0.1}$ Ga $_{0.9}$ As and Al $_{0.2}$ Ga $_{0.8}$ As, labeled as QW1 and QW2, respectively. QW1 is separated from the emitter and QW2 by 6-nm-thick Al $_{0.35}$ Ga $_{0.65}$ As barriers. Finally, QW2 is separated from the collector by a 30-nm-thick Al $_{0.35}$ Ga $_{0.65}$ As barrier.

Applying a voltage bias between the two contacts induces a nonequilibrium carrier-transport regime, which typically results in two different temperatures for the lattice and electrons. Indeed, this transport being filtered in energy thanks to tunneling and thermionic processes leads to the temperature of electrons being controlled by evaporative cooling [16] while the lattice temperature is controlled by transfer of energy from the lattice to the electron bath through electron-phonon scattering [15].

The theoretical study of such physical processes for a realistic device requires consideration of both electron and phonon transport. To do this, we use an inhouse code in which electron and heat transport are solved self-consistently. We subsequently use virtual Büttiker probes to unambiguously determine the local electronic temperature and electrochemical potential inside the device.

### A. Electron-transport model

A description of the method used to calculate electron and heat transport in this work has been thoroughly presented in a previous work [19]. The equations required for the analysis presented herein will nonetheless be recalled.

Let us first introduce the retarded Green’s function at energy  $E$  and transverse wavevector  $k_t$ :

$$G_{k_t}^r = [(E - V)I - H_{k_t} - \Sigma_{L,k_t}^r - \Sigma_{R,k_t}^r - \Sigma_{S,k_t}^r]^{-1}, \quad (1)$$

where  $V$  is the electrostatic potential energy, which is considered only transport-axis dependent and thus invariant

in the transverse plane;  $I$  is the identity matrix;  $H_{k_t}$  is the effective-mass Hamiltonian describing the  $\Gamma$  valley of the conduction band;  $k_t = n_{k_t} \times 2\pi/L_t$  is the transverse wavevector, with  $n_{k_t}$  an integer and  $L_t$  the perpendicular dimension of the system;  $\Sigma_{L(R),k_t}^r$  are the self-energies for the left ( $L$ ) and right ( $R$ ) semi-infinite device contacts;  $\Sigma_{S,k_t}^r$  is the self-energy calculated within the self-consistent Born approximation, which accounts for the interactions between electrons and both acoustic and polar-optical phonons. In our approach, acoustic and polar-optical phonon baths are considered at equilibrium and locally follow a Bose-Einstein distribution. They are not, however, in equilibrium with one another. We thus need to define two different temperatures  $T_{AC}$  and  $T_{OP}$ , those of acoustic and polar-optical phonons, respectively. The physical reason for this is that the imbalance in their respective energy densities leads to the net anharmonic decay of optical phonons into acoustic ones, which has a critical impact on the thermal transport [20]. These temperatures are self-consistently computed by coupling the electron-transport equations with the heat equation, as presented in Sec. II B.

The lesser/greater Green's functions are obtained by deriving the retarded Green's functions using the following identities:

$$G_{k_t}^{\lessgtr} = G_{k_t}^r (\Sigma_{L,k_t}^{\lessgtr} + \Sigma_{R,k_t}^{\lessgtr} + \Sigma_{S,k_t}^{\lessgtr}) G_{k_t}^{r\dagger}, \quad (2)$$

$$\Sigma^r = \frac{1}{2} [\Sigma^> - \Sigma^<], \quad (3)$$

where the total scattering self-energy for a given mode  $k_t$  can be decomposed into

$$\Sigma_{S,k_t}^{\lessgtr} = \Sigma_{AC,k_t}^{\lessgtr} + \Sigma_{POP,k_t}^{\lessgtr}, \quad (4)$$

in which  $\Sigma_{AC,k_t}^{\lessgtr}$  is the self-energy for acoustic phonons calculated within the elastic assumption at position  $j$  along the transport axis. This can be expressed as [21,22]

$$\begin{aligned} \Sigma_{AC}^{\lessgtr}(j, j; E) &= \sum_{k_t'} \pi (2n_{k_t'} + 1) \frac{\Xi^2 k_B T_{AC}(j)}{\rho u_s^2} (j) \\ &\times G_{k_t'}^{\lessgtr}(j, j; E), \end{aligned} \quad (5)$$

where  $\Xi$  is the deformation potential,  $\rho$  is the mass density,  $u_s$  is the sound velocity, and  $T_{AC}$  is the temperature of acoustic phonons. We assume interactions with acoustic phonons to be local and therefore only consider the diagonal part of the Green's function [23].

The scattering self-energy for polar-optical phonons is defined in Eq. (6), and we use the diagonal expression proposed in a previous work by Moussavou *et al.* to effectively

describe their long-range interactions [24]. For a given wavevector  $k_t$ , we have

$$\begin{aligned} \Sigma_{POP,k_t}^{\lessgtr}(j, j; E) &= \frac{\lambda M^2}{2\pi S} \sum_{k_t'} [(n_L(j) + 1) G_{k_t'}^{\lessgtr}(j, j; E \pm \hbar\omega_{LO}) \\ &+ (n_L(j)) G_{k_t'}^{\lessgtr}(j, j; E \mp \hbar\omega_{LO})] \\ &\times \int_{\pi/L_t}^{\pi} \frac{\pi (2n_{k_t'} + 1)}{\sqrt{(k_t - k_t' \cos \theta)^2 + (k_t' \sin \theta)^2}} d\theta, \end{aligned} \quad (6)$$

where  $n_L(j) = (e^{\hbar\omega_{LO}}/(k_B T_{POP}) - 1)^{-1}$ , in which  $\hbar\omega_{LO}$  the LO phonon energy and  $T_{POP}$  the phonon temperature,  $M$  is the Fröhlich factor,  $\theta$  is the angle between  $k_t$  and  $k_t'$ , and  $\lambda$  is a scaling factor correcting for the reduced strength emerging from the diagonal approximation. The value  $\lambda = 8$  used in this paper has been obtained using the physically based analytical model developed in Ref. [24].

Once the Green's functions are obtained, we have access to all the physical properties of interest. The electron density  $n_j$  at position  $j$  along the transport axis is given by

$$n_j = -2 \times \frac{i}{2\pi} \int G_{j,j}^<(E) dE, \quad (7)$$

with  $G_{j,j}^<(E) = \sum_{k_t} \pi (2n_{k_t} + 1) G_{k_t,j,j}^<(E)$ . The electron current density (in A/m<sup>2</sup>)  $J_{j \rightarrow j+1}$  from position  $j$  to  $j + 1$  is

$$J_{j \rightarrow j+1} = \int \mathcal{J}_{j \rightarrow j+1}(E) dE, \quad (8)$$

where  $\mathcal{J}_{j \rightarrow j+1}(E)$  is the electron current density spectrum [in A/(m<sup>2</sup> eV)]:

$$\begin{aligned} \mathcal{J}_{j \rightarrow j+1}(E) &= \frac{e}{\hbar} \sum_{k_t} \frac{2n_{k_t} + 1}{S} [H_{j,j+1} G_{k_t,j+1,j}^<(E) \\ &- G_{k_t,j,j+1}^<(E) H_{j+1,j}]. \end{aligned} \quad (9)$$

We can then deduce the electronic energy current, which reads

$$J_{j \rightarrow j+1}^E = \int \frac{E}{e} \mathcal{J}_{j \rightarrow j+1}(E) dE. \quad (10)$$

The first derivative of the electronic energy current corresponds to the cooling power density (in W/m<sup>3</sup>):

$$Q_j = -\nabla_j \cdot J_j^E, \quad (11)$$

where  $Q_j$  is the source term allowing coupling of the electron-transport equations to the heat equation. A negative value of  $Q_j$  corresponds to an increase of the electronic

energy current density and then to a transfer of energy from the lattice to the electron bath, leading to a cooling of the lattice. A positive value corresponds to the opposite phenomenon, i.e., the heating of the lattice.

### B. Heat-transport model

The lattice temperature is computed by solving the one-dimensional heat equation along the direction of transport. The discretized heat equation at site  $j$  can be expressed as

$$\left[ -\frac{\partial}{\partial x} [\kappa_{\text{th}}(x) \frac{\partial}{\partial x} T_{\text{AC}}(x)] \right]_j = Q_j. \quad (12)$$

Here, the thermal conductivity of the material  $\kappa_{\text{th}}$  is taken as being equal to 4 W/(mK) in the QW region to take into account the increased thermal resistance emerging from the interface between layers [25,26]; in the rest of the device, it is set to the bulk value of GaAs (46 W/(mK)). The temperature considered in the heat equation  $T_{\text{AC}}$  is the temperature of acoustic phonons; they have a larger velocity than their optical counterpart and are therefore mainly responsible for heat transport [27]. The left and right contact temperatures are set to  $T_{\text{AC}} = 300$  K by enforcing Dirichlet boundary conditions. This assumption corresponds to considering massive contacts with a sufficiently high thermal capacitance. Here  $Q_j$  is the cooling power density previously defined [see Eq. (11)], which ensures local energy conservation between the electron and phonon systems. From a physical point of view, since the acoustic phonons have much lower energy than the energy range of interest, their interactions with electrons are assumed to be elastic. This implies that electrons lose or increase their energy by scattering with polar-optical phonons. In turn, optical phonons decay into acoustic phonon modes, which sustains the thermal-energy propagation along the device. In stationary conditions, the power transfer from optical to acoustic phonons must be equal to the cooling power density  $Q_j$ . Within a relaxation-time approximation, we can thus write

$$\frac{[T_{\text{POP}}(j) - T_{\text{AC}}(j)]C_{\text{POP}}}{\tau_{\text{POP} \rightarrow \text{AC}}} = Q_j, \quad (13)$$

where  $\tau_{\text{POP} \rightarrow \text{AC}}$  is the relaxation time of polar-optical phonons into acoustic phonons ( $\tau_{\text{POP} \rightarrow \text{AC}} = 4.16 \times 10^{-12}$  s) and  $C_{\text{POP}}$  is the thermal capacitance of polar optical phonons per unit volume [ $C_{\text{POP}} = 1.72 \times 10^6$  J/(m<sup>3</sup> K)]. The numerator of the left-hand side expresses the average energy per unit volume exchanged between the polar-optical and acoustic phonon baths in an interval  $\tau_{\text{POP} \rightarrow \text{AC}}$ . Equation (13) allows us to compute  $T_{\text{POP}}(j)$  from the knowledge of  $Q_j$  and  $T_{\text{AC}}(j)$ . The computed values of  $T_{\text{AC}}$  and  $T_{\text{POP}}$  are substituted into Eqs. (5) and (6). This establishes the coupling between the heat equation and

the electron-transport equations. The heat equation is iteratively solved together with the transport equations and the Poisson equation, until the criteria of convergence for both electron density and carrier current density are reached. The potential energy  $V$  is self-consistently determined by nonlinearly coupling the transport equations with the Poisson equation through the electron density.

### C. Local electron temperature

As a postprocessing step, we use the virtual Büttiker probe [28,29] to calculate the local electron temperature. This is based on the introduction of a local noninvasive probe defined at position  $j$  by its self-energy:

$$\begin{aligned} \Sigma^>(j, j; E) &= -i[1 - f_{\text{FD}}(E, \mu_j, T_j)] \\ &\times i \left[ \frac{G^>(j, j; E) - G^<(j, j; E)}{2\pi} \right] \times v_{\text{coup}}, \end{aligned} \quad (14)$$

$$\begin{aligned} \Sigma^<(j, j; E) &= if_{\text{FD}}(E, \mu_j, T_j) \\ &\times i \left[ \frac{G^>(j, j; E) - G^<(j, j; E)}{2\pi} \right] \times v_{\text{coup}}, \end{aligned} \quad (15)$$

where  $f_{\text{FD}}(E, \mu_j, T_j)$  is the Fermi-Dirac distribution of the probe, which depends on the electrochemical potential  $\mu_j$  and the electronic temperature  $T_j$ , and  $i\{[G_{j,j}^>(E) - G_{j,j}^<(E)]/2\pi\}$  is the local density of states, which is common to the probe and the device.

Using the previously determined Green's functions of the device, we calculate the electron and energy currents between the probe and the device:

$$(\Delta I_e)_j \equiv \int_0^\infty [\Sigma_{j,j}^>(E)G_{j,j}^<(E) - G_{j,j}^>(E)\Sigma_{j,j}^<(E)] dE, \quad (16)$$

$$(\Delta I_q)_j \equiv \int_0^\infty \frac{E}{e} [\Sigma_{j,j}^>(E)G_{j,j}^<(E) - G_{j,j}^>(E)\Sigma_{j,j}^<(E)] dE. \quad (17)$$

The principle now is to find  $[T_j; \mu_j]$  such that  $(\Delta I_e)_j$  and  $(\Delta I_q)_j$  vanish. The probe is then in a local equilibrium with the device, itself arbitrarily out of equilibrium. The temperature and chemical potential of the probe are therefore accurate measurements of the thermodynamic properties of the device. To find the vanishing conditions of the currents in each point of the device, we solve Eqs. (16) and (17) as a pair of coupled nonlinear equations using a Newton-Raphson algorithm.

This method determines the electronic temperature and electrochemical potential in systems arbitrarily far from equilibrium provided the probe is localized, weak, and broadband, ensuring that the properties of the device are



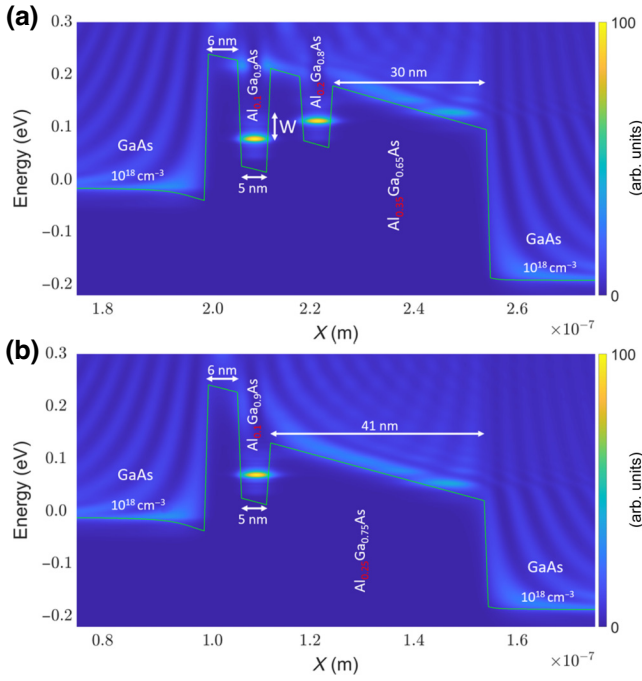


FIG. 2. Local density of states (colormap) and potential profile (green solid line) of (a) an SQW and (b) a QCC for a voltage bias of  $V = 0.175$  V. The QCC is obtained from the parameters of Fig. 1. The zero of energy is set to the emitter Fermi energy.

measured while avoiding perturbation by the probe [28]. These conditions being satisfied by the proposed probe, it is expected to yield unique and unambiguous values of electronic temperature and chemical potential. In the next section, we restrict ourselves to the study of the electronic temperature based on this approach.

### III. RESULTS AND DISCUSSION

In this section, we analyze the physical properties of the QCC whose local density of states and potential profile are represented in Fig. 2(a). We can clearly see that the structure parameters taken in Fig. 1 lead to the desired steplike feature of the QW states. We also compare its properties with those of the single-quantum-well (SQW) structure whose local density of states and potential profile are represented in Fig. 2(b).

#### A. Electron temperatures

In this section, we explain the behaviors of the electronic temperatures in each QW of the structure. Figure 3 shows the electron temperatures in QW1 and QW2 as functions of the applied bias. We observe a phase opposition of oscillations between these two temperatures. Figure 3 also shows  $W$ , the energy difference between the two QW ground states. We see that the period of oscillations corresponds to the polar-optical phonon energy  $\hbar\omega_{\text{LO}}$ , equal to 35 meV [30]. To explain these dependencies, we

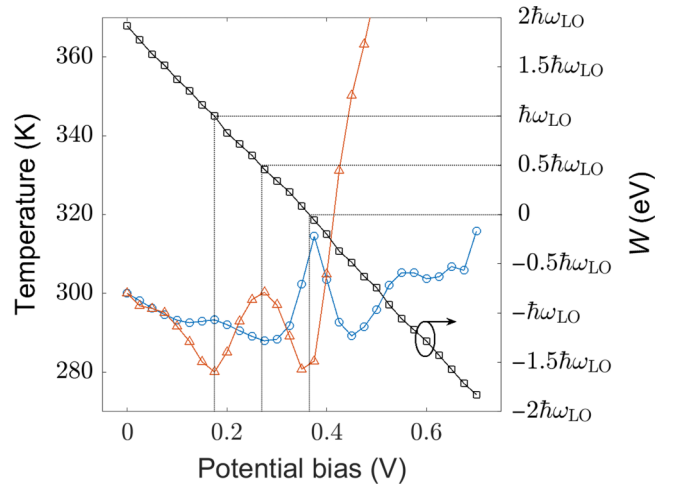


FIG. 3. Representation of the calculated electronic properties as a function of bias, showing: the average temperature of the electrons in the first (blue line with circle markers) and second QW (orange line with triangle markers);  $W$ , the energy difference between the first and second QWs' ground states (black line with square markers).

analyze the injected and extracted current spectra impacting the electron distributions in each QW.

The first extrema of electron temperatures, at  $V = 0.175$  V, correspond to  $W \approx \hbar\omega_{\text{LO}}$ . At this bias, Fig. 4(a) shows that the current density spectra [see Eq. (9)] from the emitter to QW1 and from QW1 to QW2 exhibit maxima that are separated by the polar-optical-phonon energy  $\hbar\omega_{\text{LO}}$ . Moreover, in Fig. 4(b), which shows the first subband of the two QWs, we can see that the energy difference between the ground states of the two QWs is also equal to  $\hbar\omega_{\text{LO}}$ . This ensures that the intersubband transition between the two ground states is principally controlled by LO phonon absorption. Indeed, since  $W > k_B T \approx 25$  meV, most thermally excited electrons cannot directly tunnel from QW1 to QW2 through elastic scattering processes. Due to the broad injection coming from the emitter, alongside the lack of selective extraction of thermally excited electrons, the distribution of electrons in QW1 becomes hotter. Conversely, due to the effective injection of electrons assisted by LO phonon absorption near the ground state of QW2, followed by the thermionic extraction of electrons above the last thick AlGaAs barrier, the distribution of electrons in QW2 becomes colder. As a result, in Fig. 4(c), which shows the electron density spectra in the QWs, QW1 (QW2) exhibits a broader (narrower) distribution, consistent with a higher (lower) electron temperature.

At  $V = 0.275$  V, the energy difference between the two subbands  $W \approx \frac{1}{2}\hbar\omega_{\text{LO}}$ . We can see in Fig. 5(a), which shows electron current density spectra for both QWs, that the maximum of injection into QW2 now happens  $\frac{1}{2}\hbar\omega_{\text{LO}}$  above the QW2 ground state. Although the absorption of one LO phonon by electrons in QW1 can only lead to

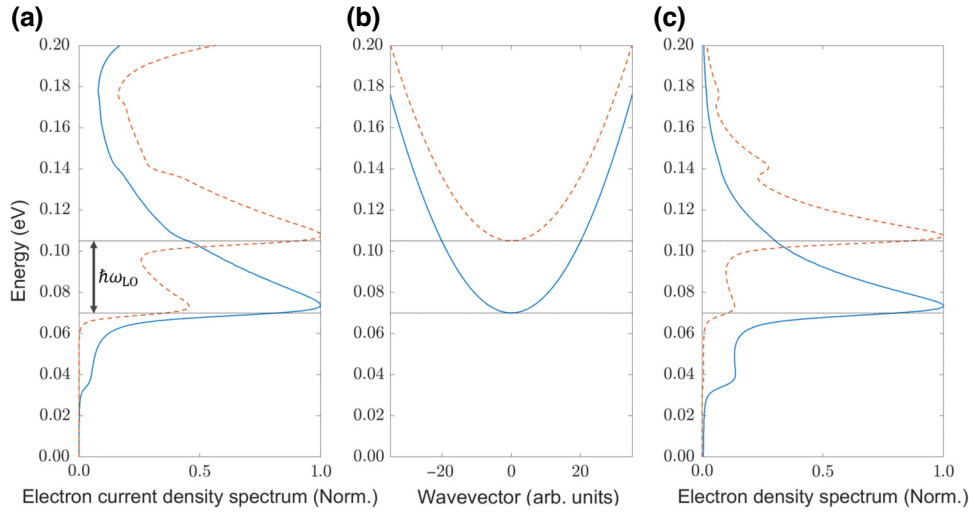


FIG. 4. (a) Normalized electron current density spectrum in the first QW (blue solid line) and between both QWs (orange dashed line). Here  $V = 0.175$  V. (b) First subband for the first (blue solid line) and second QW (orange dashed line) represented as functions of the transverse wavevector,  $k_t$ . (c) Electron density spectrum for the first (blue solid line) and second QW (orange dashed line). In all subfigures, the ground states of the first subbands of both QWs are also represented (horizontal dotted lines across each).

this energy or higher, the presence of a peak at the QW2 ground-state energy demonstrates that another scattering mechanism occurs. Figure 5(b) shows the first subband of the two QWs. Here, we can see that since  $W$  is equal to  $\frac{1}{2}\hbar\omega_{LO}$ , the minimum change in wavevector required for the intersubband transition assisted by LO phonons is nonzero. Due to the wavevector dependency in the polar-optical phonon self-energy [see Eq. (6)], the LO phonon absorption is less efficient than in the previous case (i.e.,  $V = 0.175$  V). Moreover, the value of  $W$  is now less than  $k_B T$ , leading to a substantial fraction of the thermally excited electrons being able to tunnel via elastic scattering with acoustic phonons. This possible extraction of thermally excited electrons via elastic scattering processes thus induces a local minimum of electron temperature in QW1. Finally, in Fig. 5(c), which shows the electron density spectra in QW1 and QW2, we can see that the electron density spectrum in QW2 exhibits two peaks: one is located near the QW2 ground state, and the other is  $\frac{1}{2}\hbar\omega_{LO}$  above the QW2 ground state, corresponding to the energy of the shifted maximum of current. This provides evidence that the energy-selective injection resulting from electron-phonon interactions shapes the electron distribution and thus the electron temperature. The injection of electrons into QW2 at this energy resulting from LO phonon absorption thus leads to a local maximum of electron temperature in QW2.

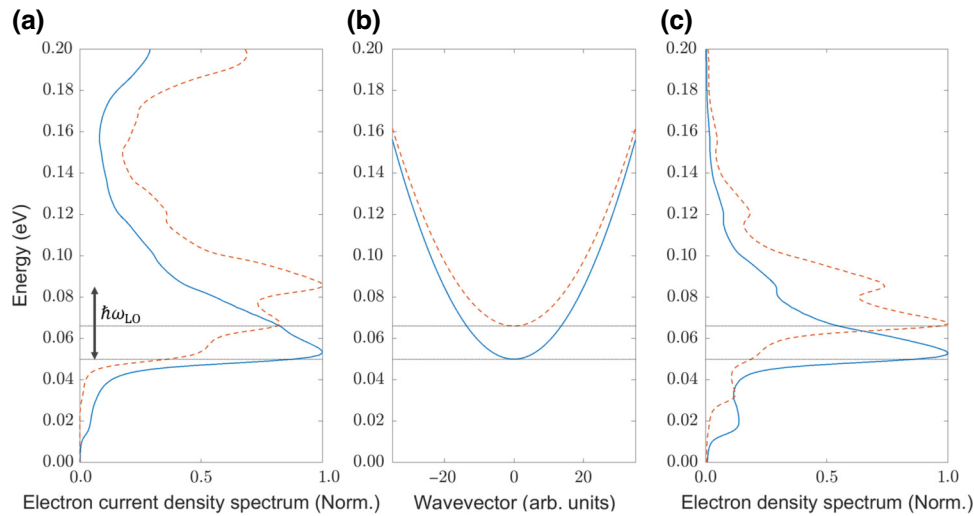
Finally, at  $V = 0.375$  V,  $W \approx 0$ , which is the resonant case, in which the QW ground states are aligned. Unlike for the two previous biases, electrons near the QW1 ground-state energy do not need to absorb phonons to flow from QW1 to QW2. In Fig. 6(a), which shows the electron current density spectra from the emitter to QW1 and from

QW1 to QW2, we can see that the current density spectrum gets narrower between the injection into QW1 and the injection into QW2. This narrowed injection stems from the fact that electrons in QW1 that are 35 meV above the ground state can now emit LO phonons to get injected into QW2. However, as can be seen in Fig. 6(b), which shows the first subband of the two QWs, electrons of QW1 below this energy are forbidden to emit LO phonons, as this would result in an injection below the QW2 ground state. In Fig. 6(c), which shows the electron density spectra in both QWs, we can see that this narrow energy range acts as a bottleneck for electrons in QW1 and leads to the appearance of a shoulder at 0.055 eV. This is consistent with the fact that this configuration corresponds to a maximum of temperature for electrons in QW1. Conversely, the narrow injection into QW2, along with the subsequent thermionic emission above the last thick AlGaAs barrier, leads to a distribution of electrons corresponding to a lower temperature.

Above  $V = 0.375$  V, in Fig. 4, we observe a fast increase of the temperature in QW2. Since  $W$  becomes negative, electrons are injected into QW2 at energies above the ground state. On the other hand, the electron temperature in QW1 remains closer to 300 K until a bias of 0.65 V is reached, for which QW1's ground state becomes lower than the emitter's conduction-band edge, where the same phenomenon happens.

## B. Cooling properties

In this section, we compare the cooling properties of the present QCC to its SQW counterpart. To faithfully compare the two structures, we consider an SQW device of the

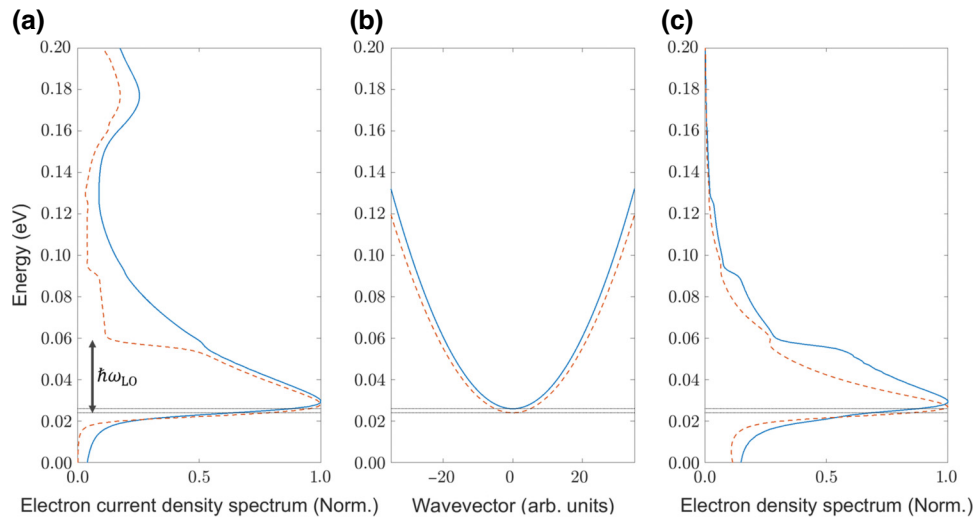
FIG. 5. Same as Fig. 4 for  $V = 0.275$  V.

same length, in which the energy gap between the emitter Fermi level and the first QW state is conserved at equilibrium. Moreover, the energy interval between the QW level and the top of the second barrier is taken as being identical to that between the level of the second QW and the last barrier of the QCC. To do this, we replace the second barrier, the second QW, and the last barrier of the QCC by a single 41-nm-thick barrier of  $\text{Al}_{0.25}\text{Ga}_{0.75}\text{As}$ . The new structure's local density of states and potential profile are represented in Fig. 2(b) for a bias of  $V = 0.175$  V.

By integrating the negative part of the cooling power density  $Q_j$  [see Eq. (11)] over  $x$  (the direction of transport), as represented by the orange area in Fig. 7, we obtain the cooling power  $J_Q$  of the central region (between the middle of the first barrier and the end of the last barrier). This quantity is represented for both devices in Fig. 8(a). We

also represent the contributions of QW1 and QW2 to the cooling power for the QCC. This cooling power is obtained by integrating the negative part of the cooling power density  $Q_j$  [see Eq. (11)] over  $x$  (the direction of transport), as represented in Fig. 7. Of course, integrating both the negative and positive components of  $Q_j$  over the whole device systematically yields a positive value equal to the supplied electrical power ( $P_{\text{Supplied}} = J \times V$ ). This corresponds to an overall heating of the device. As we are studying the cooling of the QW region of the device, we restrict ourselves to the calculation of the heat transferred in its central region.

We can first see that the QCC yields lower cooling power than the SQW structure for biases below  $V = 0.175$  V; however, its maximum cooling power is much greater. Indeed,  $J_Q = 383 \text{ kW/m}^2$  at  $V = 0.3$  V for the

FIG. 6. Same as Figs. 4 and 5 for  $V = 0.375$  V.

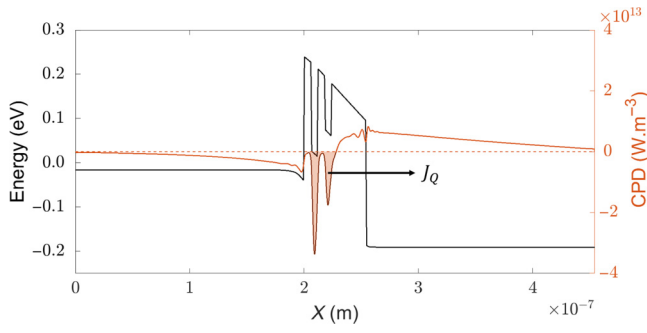


FIG. 7. Potential profile (black line) and cooling power density  $Q_j$  (orange solid line) for a voltage bias of  $V = 0.175$  V. The base line (orange dashed line) and the cooling power ( $J_Q$ ) are also represented. The zero of energy is set to the emitter Fermi energy.

QCC, whereas the maximum is only  $244 \text{ kW/m}^{-2}$  at  $V = 0.25$  V for the SQW. Similar to the temperature of the electrons, the QCC cooling power depicts oscillations. These oscillations have their origins in the phenomena described in the previous section. This can be directly deduced from QW1's and QW2's contributions to the QCC cooling power, which are locally maximized at biases corresponding to local minima of electronic temperature [see Fig. 3]. The overall maximum cooling power is obtained for  $W \approx 0.5\hbar\omega_{LO}$ , where both QWs contribute to the cooling.

Figure 8(b) shows the corresponding coefficient of performance (COP), which is defined as the ratio between

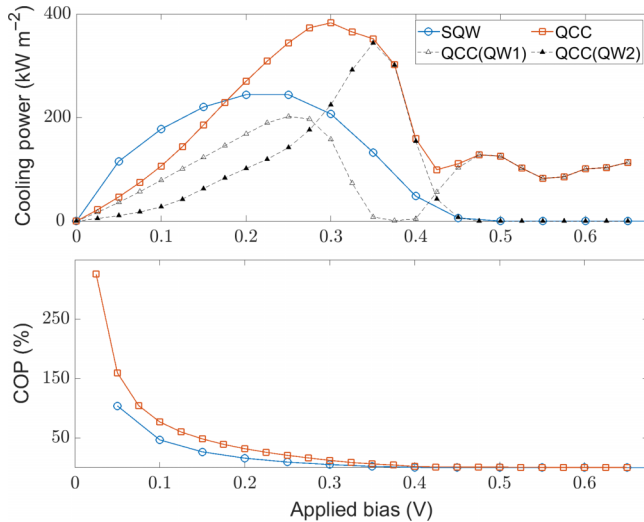


FIG. 8. (a) Cooling power  $J_Q$  as a function of potential bias for the SQW (blue line with circle markers) and the QCC (orange line with square markers). Contributions of QW1 and QW2 to the cooling power are also represented (black dashed lines with hollow and filled triangle markers, respectively). (b) Coefficient of performance (COP) as a function of the potential bias for the SQW (blue line with circle markers) and the QCC (orange line with square markers).

$J_Q$  and  $P_{\text{Supplied}}$ . For both structures, the COP decreases with the bias, as is unfortunately usual in thermionic cooling devices (see Fig. 4 in Ref. [31]). However, for all biases, the COP of the QCC is significantly higher than the COP of the SQW structure. This result shows that for the same flux of electrons, more phonons are absorbed in the QCC than in the SQW structure, which is exactly the purpose of the QCC. Here, although the applied bias required to achieve maximum cooling power in the QCC is higher than that required for the SQW structure, the COP at maximum  $J_Q$  is higher for the QCC (12.3%) than for the SQW structure (9.3%).

The QCC shows an overall greater efficiency and greater  $J_Q$  than its SQW counterpart. There is, however, no significant reduction of the lattice temperature. This is due to the huge difference between the heat capacities of electrons and phonons. To solve this problem, one would need to increase the numbers of electrons in the QW regions. This could be achieved by heavily doping of the order of  $10^{21}$ – $10^{22} \text{ cm}^{-3}$  or by considering metal-semiconductor junctions. This is, however, outside the scope of this article.

#### IV. CONCLUSIONS

In the present work, we theoretically investigate the proposed quantum cascade cooler device through the use of an inhouse quantum code coupling heat and electron transport. We report anticorrelated electronic temperature oscillations as a function of voltage bias between two successive QWs. We show that this behavior directly emerges from the ability of electrons to absorb or emit polar-optical phonons whose energy (35 meV) establishes the period of oscillations. The bias dependence in the proposed heterostructure sheds light on the versatile physical properties that can emerge from this kind of device. The thermal properties of this device are also compared to its single-quantum-well counterpart. We show that the QCC leads to significant improvements in both maximum cooling power and efficiency, and it is therefore a good candidate for solid-state cooling upon optimization. The present QCC cooling structures may be also useful in devices in which electronic cooling plays an important role. Light-emitting devices will gain better efficiency if the carrier temperature can be decreased via our cooling device by 30–50 K. Non-radiative losses due to thermal escape of carriers outside the confining potential wells would be decreased. Similarly, in QW infrared photodetectors, the dark current will be reduced by cooling electrons in the QW. These are only a few examples; we believe that there will be many more useful applications of electron cooling.

#### ACKNOWLEDGMENT

This work was supported by the GELATO project from ANR (ANR-21-CE50-0017).



- [1] A. Habibi Khalaj, T. Scherer, and S. K. Halgamuge, Energy, environmental and economical saving potential of data centers with various economizers across Australia, *Appl. Energy* **183**, 1528 (2016).
- [2] J. Ni and X. Bai, A review of air conditioning energy performance in data centers, *Renewable Sustainable Energy Rev.* **67**, 625 (2017).
- [3] B. Whitehead, D. Andrews, A. Shah, and G. Maidment, Assessing the environmental impact of data centres part 1: Background, energy use and metrics, *Build. Environ.* **82**, 151 (2014).
- [4] L. Xiu, Time Moore: Exploiting Moore's Law from the perspective of time, *IEEE Solid-State Circuits Mag.* **11**, 39 (2019).
- [5] C. A. Mack, Fifty years of Moore's Law, *IEEE Trans. Semicond. Manuf.* **24**, 202 (2011).
- [6] G. E. Moore, Lithography and the future of Moore's Law, *IEEE Solid-State Circ. Soc. Newsl.* **11**, 37 (2006).
- [7] Q. Zhang, K. Deng, L. Wilkens, H. Reith, and K. Nielsch, Micro-thermoelectric devices, *Nat. Electron.* **5**, 333 (2022).
- [8] J. Mao, G. Chen, and Z. Ren, Thermoelectric cooling materials, *Nat. Mater.* **20**, 454 (2021).
- [9] Y.-H. Gong, J. J. Yoo, and S. W. Chung, Thermal modeling and validation of a real-world mobile AP, *IEEE Design & Test* **35**, 55 (2018).
- [10] C. Fiegna, Y. Yang, E. Sangiorgi, and A. G. O'Neill, Analysis of self-heating effects in ultrathin-body SOI MOSFETs by device simulation, *IEEE Trans. Electron. Devices.* **55**, 233 (2008).
- [11] R. Gaska, A. Osinsky, J. Yang, and M. Shur, Self-heating in high-power AlGaIn-GaN HFETs, *IEEE Electron Device Letters* **19**, 89 (1998).
- [12] E. Pop, S. Sinha, and K. Goodson, Heat generation and transport in nanometer-scale transistors, *Proceedings of the IEEE* **94**, 1587 (2006).
- [13] K. M. Kretzschmar and D. R. Wilkie, The use of the Peltier effect for simple and accurate calibration of thermoelectric devices, *Proc. R. Soc. Lond., B., Biol. Sci.* **190**, 315 (1975).
- [14] E. L. Murphy and R. H. Good, Thermionic emission, field emission, and the transition region, *Phys. Rev.* **102**, 1464 (1956).
- [15] G. N. Hatsopoulos and E. P. Gyftopoulos, *Theory, Technology, and Application*, Thermionic Energy Conversion, Vol. 2 (MIT Press, Cambridge, Mass, 1979).
- [16] A. Yangui, M. Bescond, T. Yan, N. Nagai, and K. Hirakawa, Evaporative electron cooling in asymmetric double barrier semiconductor heterostructures, *Nat. Commun.* **10**, 4504 (2019).
- [17] K. A. Chao, M. Larsson, and A. G. Mal'shukov, Room-temperature semiconductor heterostructure refrigeration, *Appl. Phys. Lett.* **87**, 022103 (2005).
- [18] J. Faist, F. Capasso, D. L. Sivco, C. Sirtori, A. L. Hutchinson, and A. Y. Cho, Quantum cascade laser, *Science (New York, NY)* **264**, 553 (1994).
- [19] M. Bescond, G. Dangoisse, X. Zhu, C. Salhani, and K. Hirakawa, Comprehensive analysis of electron evaporative cooling in double-barrier semiconductor heterostructures, *Phys. Rev. Appl.* **17**, 014001 (2022).
- [20] J. Lai and A. Majumdar, Concurrent thermal and electrical modeling of sub-micrometer silicon devices, *J. Appl. Phys.* **79**, 7353 (1996).
- [21] C. Jacoboni and L. Reggiani, The Monte Carlo method for the solution of charge transport in semiconductors with applications to covalent materials, *Rev. Mod. Phys.* **55**, 645 (1983).
- [22] S. Jin, Y. Park, and H. Min, A three-dimensional simulation of quantum transport in silicon nanowire transistor in the presence of electron-phonon interactions, *J. Appl. Phys.* **99**, 123719 (2006).
- [23] M. Bescond, H. Carrillo-Nuñez, S. Berrada, N. Cavassilas, and M. Lannoo, Size and temperature dependence of the electron-phonon scattering by donors in nanowire transistors, *Solid-State Electron.* **122**, 1 (2016).
- [24] M. Moussavou, M. Lannoo, N. Cavassilas, D. Logoteta, and M. Bescond, Physically based diagonal treatment of the self-energy of polar optical phonons: Performance assessment of III-V double-gate transistors, *Phys. Rev. Appl.* **10**, 064023 (2018).
- [25] A. Sood, J. A. Rowlette, C. G. Caneau, E. Bozorg-Grayeli, M. Asheghi, and K. E. Goodson, Thermal conduction in lattice-matched superlattices of InGaAs/InAlAs, *Appl. Phys. Lett.* **105**, 051909 (2014).
- [26] M. N. Luckyanova, J. A. Johnson, A. A. Maznev, J. Garg, A. Jandl, M. T. Bulsara, E. A. Fitzgerald, K. A. Nelson, and G. Chen, Anisotropy of the thermal conductivity in GaAs/AlAs superlattices, *Nano Lett.* **13**, 3973 (2013).
- [27] E. Pop, R. Dutton, and K. Goodson, in *International Conference on Simulation of Semiconductor Processes and Devices, 2003. SISPAD 2003* (IEEE, Boston, Massachusetts, 2003), p. 121.
- [28] A. Shastri and C. A. Stafford, Temperature and voltage measurement in quantum systems far from equilibrium, *Phys. Rev. B* **94**, 155433 (2016).
- [29] C. A. Stafford, Local temperature of an interacting quantum system far from equilibrium, *Phys. Rev. B* **93**, 245403 (2016).
- [30] M. Lundstrom, *Fundamentals of Carrier Transport*, Cambridge Books Online (Cambridge University Press, 2000).
- [31] M. Bescond and K. Hirakawa, High-performance thermionic cooling devices based on tilted-barrier semiconductor heterostructures, *Phys. Rev. Appl.* **14**, 064022 (2020).